HiSST: 2nd International Conference on
High-Speed Vehicle Science Technology
11–15 September 2022, Bruges, Belgium

High Fidelity Numerical Simulations of Combustion for Airbreating Engines

Christer Fureby[1]

Abstract

Large Eddy Simulation (LES) has rapidly developed into a powerful computational methodology for fluid dynamic studies, between Reynolds Averaged Navier Stokes (RANS) and Direct Numerical Simulation (DNS) in both accuracy and cost. High-speed combustion applications, such as ducted rockets, ramjets, scramjet, dual-mode ramjets, and rotating detonation engines, are very interesting propulsion systems, but also challenging to analyze and develop. Up to about a decade ago we were limited to use experimental facilities, equipped with advanced conventional and non-intrusive diagnostic tools to study such flows. The main drawback besides the cost of such studies is the limited field-of-view, and the challenges understanding the whole flow. With the increase in computational capacity seen over the last decade, we now have the possibility of using RANS, LES and DNS to analyze these flows in detail. RANS has been around for a long time, it's advantages and disadvantages being well known while DNS is only suited for canonical flows due to its very high computational cost. LES on the other hand, have the potential to be used together with experiments to provide detailed insight into the flow physics, and at the same time facilitating various design aspects associated with the flow physics. Here, the concept of LES for high-speed combustion is reviewed, and examples of LES results are discussed.

1. Introduction and Background

During the past decade Large Eddy Simulation (LES), [1-3], which is a compromise between Direct Numerical Simulation (DNS), [4], and Reynolds Averaged Navier-Stokes (RANS) methods, [5], has been successfully used to study high-speed combustion applications, e.g. [6-15]. In LES, turbulent scales larger than the grid spacing are resolved, while subgrid scales, and the effect they have on the larger scales, is modeled. This allows for capturing transient phenomena such as turbulence-chemistry, shock-shock, shock boundary-layer and shock-flame interactions. The increasing number of successful LES, with many demonstrating excellent qualitative and quantitative agreement with data, makes LES a well-accepted method in both academia and industry. Due to the rapid advancement in high-performance computing, LES has become much more available, but physics modeling, reliability and accuracy of LES remains to be firmly established for high-speed combustion applications, e.g. [16-17].

With high-speed combustion applications we refer to systems associated with flow velocities on the order of 1 km/s together with the additional complexities of the physics of turbulence, compressibility, shock- and rarefaction-waves, convective and radiative heat-transfer and chemical reactions. With this complexity it is not surprising that ramjet, scramjet and dual-mode ramjet combustion and detonation combustion is less well understood than other propulsion systems such as jet-engines or solid propellant rockets. Many high-speed combustion models rely on inviscid steady-state stream-tube formulations of compressible reacting flows, e.g. [18-19]. These are too simple given the complex multi-physics nature of the engine types considered for future air transportation systems but are likely to be used as engineering tools in the near future. The complexity of high-speed combustion applications makes experiments very challenging and expensive to perform, usually providing only limited amount of data. For the future we envision an increasing degree of cooperation between experimental and computational work, with high-fidelity simulations and heavily instrumented experiments jointly providing huge amount of data to be processed simultaneously and in multiple ways to provide new insights in the complex physics

[1] *Lund University, Dept. of Energy Sciences, Div. of Heat Transfer, Ole Römers väg 1, P.O. Box 118, SE-221 00 Lund, Sweden, christer.fureby@energy.lth.se*

and chemistry being fundamental to these novel engine cores.

Here, we describe and discuss the physics, chemistry and numerical aspects of LES to provide a comprehensive overview of the methodology and it is advantages and disadvantages. In addition, we also provide a few examples of LES results and how they compare with experimental data to give a flavor of what can be expected from LES in terms of accuracy and information provided. The paper ends with a brief description of the projected future of LES of high-speed combustion, as well as a summary of different aspects of LES that needs to be improved for the methodology to gain even more widespread use, in particular between industrial or engineering practitioners.

2. Large Eddy Simulation Modeling

The LES modeling approach considered here is based on the implicitly filtered mass, momentum and energy equations. The low-pass filtering is used to separate the resolved scale flow (denoted by tildes and overbars, depending on if density weighted filtering or not is used) from the unresolved (subgrid) scale flow. The filtering implies that the physics on scales larger than the filter width, Δ, can be resolved, whereas the physics on scales smaller than Δ must be modeled. For a linear viscous mixture with Fourier heat conduction and Fickian diffusion the LES mass, momentum and energy equations are,

$$\begin{cases} \partial_t(\bar{\rho}) + \nabla\cdot(\bar{\rho}\widetilde{\boldsymbol{v}}) = 0 \\ \partial_t(\bar{\rho}\widetilde{Y}_i) + \nabla\cdot(\bar{\rho}\widetilde{\boldsymbol{v}}\widetilde{Y}_i) = \nabla\cdot(\boldsymbol{j}_i - \boldsymbol{b}_i) + \bar{\dot{w}}_i \\ \partial_t(\bar{\rho}\widetilde{\boldsymbol{v}}) + \nabla\cdot(\bar{\rho}\widetilde{\boldsymbol{v}}\otimes\widetilde{\boldsymbol{v}}) = -\nabla\tilde{p} + \nabla\cdot(\widetilde{\boldsymbol{S}} - \widetilde{\boldsymbol{B}}) \\ \partial_t(\bar{\rho}\widetilde{E}) + \nabla\cdot(\bar{\rho}\widetilde{\boldsymbol{v}}\widetilde{E}) = \nabla\cdot(-\tilde{p}\widetilde{\boldsymbol{v}} + \tilde{S}\widetilde{\boldsymbol{v}} + \widetilde{\boldsymbol{h}} + \Sigma_{i=1}^{N}(h_{i,f}^{\theta}\boldsymbol{j}_i) - \boldsymbol{b}_E) + \Sigma_{i=1}^{N}(\bar{\dot{w}}_i h_{i,f}^{\theta}) \end{cases} \quad (1)$$

in which ρ is the density, $\boldsymbol{v}$ the velocity, Y_i the species mass-fractions, $\boldsymbol{j}_i \approx D_i\nabla Y_i$ the species mass flux vectors, D_i the species diffusivities, $\boldsymbol{b}_i = \bar{\rho}(\widetilde{\boldsymbol{v}Y_i} - \widetilde{\boldsymbol{v}}\widetilde{Y}_i)$ the species subgrid fluxes, $\dot{w}_i = P_{ij}\dot{w}_j$ the species formation rates, P_{ij} the stoichiometric matrix and $\dot{w}_j$ the reaction rates. In the momentum equation (1_3) $p = \rho RT$ is the pressure, R the (composition dependent) gas constant, T the temperature, $\boldsymbol{S} \approx 2\mu\boldsymbol{D}_D$ the viscous stress tensor, μ the viscosity, $\boldsymbol{D}_D$ the deviatoric part of the rate of strain tensor and $\boldsymbol{B} = \bar{\rho}(\widetilde{\boldsymbol{v}\otimes\boldsymbol{v}} - \widetilde{\boldsymbol{v}}\otimes\widetilde{\boldsymbol{v}})$ the subgrid stress tensor. In the energy equation (1_4) $E = \sum_{i=1}^{N}\left(Y_i\int_{T_0}^{T}C_{p,i}dT\right) - p/\rho + v^2/2$ being the sum of the sensible enthalpy and the kinetic energy. In addition, $p\boldsymbol{v}$ is the pressure work, $\boldsymbol{S}\boldsymbol{v}$ the viscous work, $\boldsymbol{h} \approx \kappa\nabla T$ the heat flux vector, κ the thermal diffusivity, $\sum_{i=1}^{N}(\dot{w}_i h_{i,f}^{\theta})$ the chemical heat release and $\boldsymbol{b}_E = \bar{\rho}(\widetilde{\boldsymbol{v}E} - \widetilde{\boldsymbol{v}}\widetilde{E}) + (\widetilde{p\boldsymbol{v}} - \tilde{p}\widetilde{\boldsymbol{v}}) - (\widetilde{\boldsymbol{S}\boldsymbol{v}} - \widetilde{\boldsymbol{S}}\widetilde{\boldsymbol{v}})$ the subgrid energy flux. Here, D_i and κ are obtained from the viscosity, μ, using Schmidt, Sc_i, and Prandtl, Pr, numbers, [36], respectively. Equation (1) forms a set of N+5 equations, where N is the number of species, but due to the constraint $\sum_i Y_i = 1$, one species equation (here Y_{N2}) can be discarded.

2.1. LES Subgrid Flow Modeling

The subgrid stress tensor and flux vectors, or the unresolved transport terms, $\boldsymbol{B}$, $\boldsymbol{b}_E$ and $\boldsymbol{b}_i$, in the filtered transport equations (1) can be closed using many different models. Sagaut, [1], provides a comprehensive review of subgrid models for non-reactive and incompressible flows. Most often these models are extended to compressible and reactive flows using dimensional arguments. This is questionable but in the absence of experimental or direct numerical simulation data this constitutes today's standards. Based on literature surveys and testing the most useful subgrid models appears to be the Smagorinsky (SMG) model, [20], the Localized Dynamic k-equation Model (LDKM), [21], and the Hyperviscosity (HV) model, [22]. These models are all subgrid viscosity models using different approximations for the subgrid viscosity, ν_k, bulk-viscosity, β, and subgrid kinetic energy, k. More specifically, given a general expression for the subgrid stress tensor, [20-22], $\boldsymbol{B} = -2\mu_k\boldsymbol{D}_D + \bar{\rho}(\beta(\nabla\cdot\tilde{v}) - \frac{2}{3}k)\boldsymbol{I}$, the SMG model is given by $\mu_k = c_D\bar{\rho}\Delta^2\|\widetilde{\boldsymbol{D}}\|$, $\beta = 0$ and $k = c_I\Delta^2\|\widetilde{\boldsymbol{D}}\|^2$, in which $c_D = 0.012$ and $c_I = 0.007$ are model coefficients. The HV model aims to improve the modeling of shocks using combinations of shear and bulk viscosities so that $\mu_k = c_\nu\bar{\rho}\Delta^4\|\overline{(\nabla^2\|\widetilde{\boldsymbol{D}}\|)}\|$ and $\beta = c_\beta\Delta^4\|\nabla^2\widetilde{\boldsymbol{D}}\|$, in which $c_\nu = 0.025$ and $c_\beta = 5$ are model coefficients assuming that k can be absorbed into the spherical part. The LDKM model is a one-equation subgrid viscosity model with $\mu_k = c_k\bar{\rho}\Delta\sqrt{k}$, $\beta = 0$, with k satisfying a modeled transport equation of the form $\partial_t(\bar{\rho}k) + \nabla\cdot(\bar{\rho}k\widetilde{\boldsymbol{v}}) = -\boldsymbol{B}\cdot\widetilde{\boldsymbol{D}} + \nabla\cdot(\mu_k\nabla k) - c_\varepsilon\bar{\rho}k^{3/2}/\Delta$, in which c_k and c_ε are model coefficients evaluated dynamically using scale similarity. The subgrid flux vectors in the species and energy equations, $\boldsymbol{b}_E$ and $\boldsymbol{b}_i$, are modeled such that $\boldsymbol{b}_E = (\mu_k/Pr_t)\nabla E$ and $\boldsymbol{b}_i = (\mu_k/Sc_t)\nabla Y_i$, where $\mathrm{Pr_t}\approx 0.7$ and $\mathrm{Sc_t}\approx 0.85$ are the turbulent Prandtl and Schmidt numbers, respectively.

2.2. LES Combustion Modeling

The filtered species formation rates in the species transport equations, $\overline{\dot{w}_i}$, requires separate treatment in order to describe the effect of the combustion chemistry on the flow and how the turbulent mixing affects the chemistry. The main reason for this is the inherent non-linearities in temperature and species mass-fractions in the reaction rates, the wide range of scales involved, and the large number of terms that arise due to the reaction mechanism. Several methods to model the filtered species formation rates exists and they can generally be divided into:

Flamelet models which assume that the region of combustion is thin compared to the dimensions of the flow and behaves like an interface between fuel and oxidizer (in non-premixed combustion), [23], or between reactants and products (in premixed combustion), [24]. If scale-separation applies the flow and chemistry can be decoupled such that the species transport equations (1_2) may be replaced by transport equations for a mixture fraction, z, and a progress variable, c. The chemistry can then be computed and tabulated using canonical flames, resulting in a flamelet library, parameterized by z and c, and by additional variables such as p or the scalar dissipation rate, χ, so that $Y_i^{lib} = Y_i^{lib}(z, c, \dots)$. The filtered mass fractions, $\tilde{Y}_i$, can then be computed from $\tilde{z}$, $\tilde{c}$, … and Y_i^{lib} using a probabilistic approach by which $\tilde{Y}_i = \int_0^1 \int_0^1 \mathcal{P}(z,c) Y_i^{lib}(z,c) dz dc$ where $\mathcal{P} = \mathcal{P}(z,c)$ is a Probability Density Function (PDF). In practice a presumed PDF is often used, in which Beta and Gaussian functions are used for z and c, respectively. This requires two additional transport equations for the variances of the mixture fraction and progress variable z''^2 and c''^2. The source term of the progress variable, $\overline{\dot{w}_c}$, need also to be modeled, for example from analytical expressions for the flame surface density, Σ, and the laminar flame speed, s_u, or using tabulated values, [25-26]. Flamelet models are efficient but $\overline{\dot{w}_c}$ requires additional consideration and modeling to account for compressibility effects, e.g. [26].

Finite rate chemistry models are based on the species transport equations (1_2) using closure models for the filtered species formation rates, $\overline{\dot{w}_i}$, explicitly considering the underlying chemical reaction mechanism and its reaction rates. An array of LES finite rate chemistry models of varying complexity and basic assumptions are available including the Thickened Flame Model (TFM), [27], the Eddy Dissipation Concept (EDC), [28], the Fractal Model (FM), [29], the Partially Stirred Reactor (PaSR) model, [30], the Filtered Density Function (FDF), [31], the Eulerian Stochastic Fields (ESF) model, [32], and the Linear Eddy Model (LEM), [33]. Based on previous investigations, e.g. [34], we here use the EDC, FM, PaSR and ESF models as representatives of this class of LES combustion models.

The EDC model, [29], originally developed by Magnussen, [35], following the idea of Chomiak, [36], in turn based on observations by Batchelor & Townsend, [37], suggest that at high Re numbers turbulent fine structure are not uniformly distributed but concentrated in smaller localized regions. By defining the filtered mass-fractions, temperature, and species formation-rates as $\tilde{Y}_i = \gamma^* Y_i^* + (1-\gamma^*) Y_i^0$, $\tilde{T} = \gamma^* T^* + (1-\gamma^*) T^0$ and $\overline{\dot{w}_i} = \gamma^* \dot{w}_i^* + (1-\gamma_i^*) \dot{w}_i^0$, respectively, in which * and ^{0} denote values in the fine structures and surroundings, respectively, and γ^* being the fine structure volume fraction, the subgrid balance equations of mass and energy can be compactly expressed as $\bar{\rho}\left(Y_i^* - \tilde{Y}_i\right) = (1-\gamma^*)\tau^* \dot{w}_i^*$ and $\bar{\rho} \sum_{i=1}^N \left(Y_i^* h_i^* - \tilde{Y}_i \tilde{h}_i\right) = (1-\gamma^*)\tau^* \sum_{i=1}^N h_{i,f}^\theta \dot{w}_i^*$, respectively, in which τ^* is the subgrid time scale. A model of the turbulent cascade process was developed in [35] to provide estimates of $\gamma^* \approx 1.02\left(\nu/\Delta k^{1/2}\right)^{3/4}$ and $\tau^* = 1.24\left(\Delta\nu/k^{3/2}\right)^{1/2}$, respectively, closing the subgrid EDC model.

The FM model, [29], is based on the same basic assumptions as the EDC model but uses a somewhat simpler formulation $\overline{\dot{w}_i} \approx \gamma^* \dot{w}_i^{\sim}$, in which $\dot{w}_i^{\sim}$ denote the species formation rates evaluated at the LES state, i.e. $\dot{w}_i^{\sim} = \dot{w}_i\left(\bar{\rho}, \tilde{Y}_i, \tilde{T}\right)$. The fine structure volume fraction is here estimated using fractal theory so that $\gamma^* = \gamma_N (\Delta/\ell_K)^{D_3 - 3}$, in which $\gamma_N = N_{\ell,K}/N_T$ is the ratio of the number of Kolmogorov scales, $N_{\ell,K}$, to the overall number of scales, N_T, generated locally, whereas D_3 is the fractal dimension of the turbulence. Given estimates for D_3, $N_{\ell,K}$ and N_T, [29], the FM model is closed. For high Re the fine structure volume fraction asymptotically approaches the value 0.314.

The PaSR model, [30], is also based on the same assumptions as the EDC and FM models but considers the filtered species formation rates to be obtained using a bi-modal PDF, distinguishing between the fine structure and surroundings, so that $\mathcal{P} = \gamma^* \delta(\psi^*) + (1-\gamma^*)\delta(\psi^0)$. Here, $\psi \in \{\rho, Y_i, T\}$ denotes the thermochemical state. The resulting rates are $\overline{\dot{w}_i} = \int \mathcal{P}(\psi) \dot{w}_i(\psi) d\psi = \gamma^* \dot{w}_i^* + (1-\gamma^*)\dot{w}_i^0$, which can be simplified as $\overline{\dot{w}_i} \approx \gamma^* \dot{w}_i^{\sim}$ since $\dot{w}_i$ are most often negligible outside of the fine structure regions. The modeling of γ^* is based on a geometrical analysis, [30], resulting in $\gamma^* \approx \tau_c/(\tau^* + \tau_c)$, where $\tau_c \approx \delta_u/s_u$

is a global chemical time scale, whereas τ^* is based on that the fine structure area-to-volume ratio is determined by the dissipative length scale, $\ell_D = (\nu/(v'/\Delta))^{1/2}$, and that the velocity influencing this is the Kolmogorov velocity scale, v_K, such that $\tau^* = \ell_D/v_K = \sqrt{\tau_K \tau_\Delta}$. Here, $\tau_\Delta = \Delta/v'$ represents turbulent dissipation and small-scale mixing, and τ_K is the Kolmogorov time scale.

The Eulerian Stochastic Fields (ESF) model, [32], is a stochastic rather than deterministic method of representing the probability density function class of combustion models. In the ESF approach the PDF, $\mathcal{P}$, is represented by an ensemble of N_s stochastic fields with each field encompassing the N scalars, ξ_α^n for $1 \leq n \leq N_s$ and $1 \leq \alpha \leq N$. In the present work the Ito formulation of the stochastic integral is adopted, [53], and the stochastic fields evolve according to,

$$\bar{\rho} d\xi_\alpha^n + \bar{\rho}\tilde{\boldsymbol{v}} \cdot \nabla \xi_\alpha^n dt = \nabla \cdot (\Gamma \nabla \xi_\alpha^n) dt + \bar{\rho}\sqrt{\frac{2\Gamma}{\bar{\rho}}} \nabla \xi_\alpha^n \cdot d\boldsymbol{W}^n - \frac{1}{2}\bar{\rho}\frac{C_d}{\tau_k}\left(\xi_\alpha^n - \tilde{\phi}_\alpha\right) dt + \dot{w}_\alpha^n(\xi_\alpha^n) dt, \tag{2}$$

where Γ is the total diffusion coefficient, and $d\boldsymbol{W}_i^n$ the increments of a Wiener process, different for each field but independent of the spatial location. The stochastic fields given by (2) form an equivalent stochastic system to the PDF, smooth over the scale of the filter width. Following [32] eight stochastic fields are solved for each scalar variable, making this approach very expensive.

3. Numerical Methods for High-Speed Flows

Numerical methods for LES of high-speed combustion with shocks, contact discontinuities and rarefaction waves are both important and challenging. Finite Volume Methods (FVM) prevails in fluid dynamics, in particular for realistic geometries. A specific requirement is the need for low-dissipation schemes to capture most of the resolved turbulence. These schemes are, however, poorly suited to capture shocks and other flow discontinuities, and to circumvent this, methodologies such as artificial dissipation and diffusion techniques, [37], or hybrid schemes, [38], which combine two schemes within one algorithm, and blend different flux reconstruction algorithms, have been developed. Next, we briefly describe the *density-based* FVM employed in the present high speed LES combustion study.

The reactive LES equations (1) are discretized using Gauss theorem in conjunction with a multi-step time-integration scheme. The discretized continuity equation (1_1) reads,

$$\frac{1}{\Delta t}(\rho_{\mathrm{P}}^{n+1} - \rho_{\mathrm{P}}^n) + \frac{1}{\mathrm{dV_P}}\sum_{\mathrm{f}}[\rho \boldsymbol{v}]_{\mathrm{f}}^n \cdot d\boldsymbol{A}_{\mathrm{f}} = 0, \tag{3}$$

in which the subscripts denote the locations in terms of cell centers P and cell faces f, the superscripts denote the time indices, dV_p the control volume P, $d\boldsymbol{A}_{\mathrm{f}}$ the area of face f with direction along the surface normal, Δt the time-step, and the summation runs over all cell faces of P. Equation (1_3) is discretized similarly but using an operator splitting approach with an inviscid and a viscous step,

$$\begin{aligned}
&\frac{1}{\Delta t}((\rho \boldsymbol{v})_{\mathrm{P}}^* - (\rho \boldsymbol{v})_{\mathrm{P}}^n) + \frac{1}{\mathrm{dV_P}}\sum_{\mathrm{f}}[(\rho \boldsymbol{v} \otimes \boldsymbol{v}) + p\mathbf{I}]_{\mathrm{f}}^n \cdot d\boldsymbol{A}_{\mathrm{f}} = 0, \\
&\frac{1}{\Delta t}((\rho \boldsymbol{v})_{\mathrm{P}}^{n+1} - (\rho \boldsymbol{v})_{\mathrm{P}}^*) = \frac{1}{\mathrm{dV_P}}\sum_{\mathrm{f}}\left[\mu_{\mathrm{eff}} \nabla \boldsymbol{v}\right]_{\mathrm{f}}^* d\boldsymbol{A}_{\mathrm{f}} + \frac{1}{\mathrm{dV_P}}\sum_{\mathrm{f}}\left[\mu_{\mathrm{eff}}(\nabla \boldsymbol{v}^{\boldsymbol{T}} - \frac{2}{3}tr(\mathbf{DI}))\right]_{\mathrm{f}}^* d\boldsymbol{A}_{\mathrm{f}},
\end{aligned} \tag{4}$$

in which μ_{eff} is the sum of molecular and subgrid viscosities. The energy equation (1_4) is discretized by a similar operator splitting approach such that,

$$\begin{aligned}
&\frac{1}{\Delta t}((\rho E)_{\mathrm{P}}^* - (\rho E)_{\mathrm{P}}^n) + \frac{1}{\mathrm{dV_P}}\sum_{\mathrm{f}}[\rho \boldsymbol{v}\left(E + \frac{p}{\rho}\right)]_{\mathrm{f}}^n \cdot d\boldsymbol{A}_{\mathrm{f}} = \frac{1}{\mathrm{dV_P}}\sum_{\mathrm{f}}[\mu(\nabla \boldsymbol{v} + \nabla \boldsymbol{v}^{\boldsymbol{T}})\boldsymbol{v}]_{\mathrm{f}}^n \cdot d\boldsymbol{A}_{\mathrm{f}}, \\
&\frac{1}{\Delta t}((\rho e)_{\mathrm{P}}^{n+1} - (\rho e)_{\mathrm{P}}^*) = \frac{1}{\mathrm{dV_P}}\sum_{\mathrm{f}}[-\frac{\kappa_{\mathrm{eff}}}{c_V}\nabla e]_{\mathrm{f}}^* \cdot d\boldsymbol{A}_{\mathrm{f}},
\end{aligned} \tag{5}$$

in which $e = E - \boldsymbol{v}^2/2$ is the internal energy and κ_{eff} the sum of molecular and subgrid thermal diffusivities. The species transport equations (1_2) are discretized similarly such that,

$$\begin{aligned}
&\frac{1}{\Delta t}((\rho Y_i)_{\mathrm{P}}^* - (\rho Y_i)_{\mathrm{P}}^n) + \frac{1}{\mathrm{dV_P}}\sum_{\mathrm{f}}[\rho \boldsymbol{v} Y_i]_{\mathrm{f}}^n \cdot d\boldsymbol{A}_{\mathrm{f}} = 0, \\
&\frac{1}{\Delta t}((\rho Y_i)_{\mathrm{P}}^{n+1} - (\rho Y_i)_{\mathrm{P}}^*) = \frac{1}{\mathrm{dV_P}}\sum_{\mathrm{f}}[D_{\mathrm{eff}} \nabla Y_i]_{\mathrm{f}}^n \cdot d\boldsymbol{A}_{\mathrm{f}} = \frac{1}{\Delta t}((\rho \hat{Y}_i)_{\mathrm{P}}^{n+1} - (\rho \hat{Y}_i)_{\mathrm{P}}^*), \\
&\sum_{i=0}^m \left[\alpha_i \rho \hat{Y}_i\right]_p^{n+i} = \Delta t \sum_{i=1}^m [\beta_i \dot{w}_i]_P^{n+i},
\end{aligned} \tag{6}$$

in which D_{eff} is the sum of molecular and subgrid mass diffusivities. In (6_3) the combustion chemistry is treated using Strang splitting, [40, and integrated using a Rosebrock solver, [41]. The convective fluxes are reconstructed using the Kurganov central scheme, [42-43], whereas the diffusive fluxes are reconstructed using linear interpolation between neighboring cells. The inviscid equations are solved

explicitly whereas the viscous equations are solved using Gauss-Seidel, [44].

4. Combustion Chemistry

For high-speed combustion, hydrogen (H_2) and small hydrocarbon fuels, such as ethylene (C_2H_4), are favorable due to faster ignition, whereas larger hydrocarbons, such as kerosene, are favorable from an energy contents point of view. Most research studies on high-speed combustion are performed with H_2, but also C_2H_4 is sometimes considered. For simplicity, we here focus on H_2-air combustion. Following [45-46] the choice of chemical reaction mechanism is generally found to be very important for accurate and reliable LES predictions, in particular for high-speed combustion, and it is then natural to study and synthetize this aspect also for high-speed ramjet and scramjet combustion.

For H_2-air combustion, figure 1 compare experimental data and mechanism predictions for the laminar flame speed, s_u, ignition time, τ_{ign}, and extinction strain rate, σ_{ext}, for the global mechanism of Marinov (M1), [47], the skeletal mechanisms of Eklund & Stouffer (ES7), [48], Baurle & Girimaji (BG7), [49], and Davidenko *et al.* (D7), [50], the detailed mechanisms of Jachimovski (J20), [51], Alekseev *et al.* (K30), [52], Wang *et al.* (USCII), [53], as well as the pathway-centric mechanism of Zettervall & Fureby, (Z22), [46]. For τ_{ign}, figure 1a, all mechanisms examined perform similarly above 1000 K, but with deviations in the crossover regime, 850 K<T<1000 K, and below. The reaction pathways of the global and skeletal mechanisms, all neglecting the low-temperature H_2O_2 and HO_2 chemistry, are unable to reproduce the bending of τ_{ign} in the crossover region. For the detailed mechanisms this bending appears too strong, resulting in too long ignition delay times for T<900 K. The pathway-centric Z22 mechanism is however able to reproduce the τ_{ign} data across the whole range of temperatures. Concerning s_u, in figure 1b, M1 overpredicts s_u whereas ES7, BG7 and D7 all underpredicts s_u. J20, K30, USCII and Z22 all show good agreement with the experimental data. For the laminar flame temperature, T_{fl}, (not shown) all mechanisms show good agreement with each other, and with the experimental data. For σ_{ext}, figure 1c, M1 overpredicts σ_{ext}, whereas ES7, BG7 and D7 underpredict σ_{ext}. J20, K30, USCII and Z22 all show acceptable agreement with each other and with the experimental data, suggesting that these mechanisms can represent the effects associated with fluid-dynamic strain. The main difference between the detailed (J20, K30, USCII) and pathway-centric (Z22) mechanisms is the more detailed breakdown of H_2 for Z22 and the resulting larger radical pool, rendering notably improved predictions of τ_{ign} over a wide range of combustion conditions.

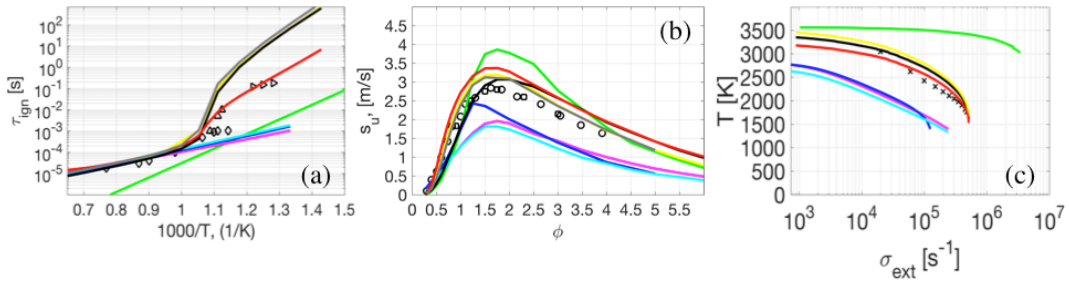

Figure 1. Comparison of (a) laminar flame speed, s_u, (b) ignition delay time, τ_{ign}, and extinction strain rate, σ_{ext}, at 1 atm for H_2-air mixtures. Legend: (—) M1, [47], (—) ES7, [48], (—) BG7, [49], (—) D7, [50], (—) J20, [51], (—) K30, [52], (—) USCII, [53], (—) Z22, [46], and experimental data (symbols) from [54-56], [57-58], and [59].

5. Examples of Supersonic Combustion LES

Here, we show results for various high-speed combustor application to demonstrate the relative importance of the different modeling aspects and to provide information about the cost and accuracy of LES for simple and advanced combustor configurations. Moreover, this section serves the purpose of demonstrating the physics disclosed in such simulations.

5.1. The Waidmann Supersonic Combustion Experiments

One of the more frequently used supersonic combustion validation cases is the supersonic combustion experiment of Waidmann *et al.*, [60-62]. Here, preheated air is expanded through a Laval nozzle entering the combustor at Ma≈2.0 and T=340 K. The combustor has a width of 40 mm, a height of 50 mm, and an upper-wall divergence angle of 3° to compensate for the boundary layer growth. A 32 mm by 6 mm strut is placed 100 mm downstream of the nozzle, and parts of combustor side-walls are made

of quartz to allow optical access. H_2 at T=250 K is injected sonically through fifteen ∅1.0 mm injectors at the strut base. The equivalence ratio is $\phi \approx 0.034$, and the experimental studies included Schlieren imaging, OH Laser Induced Fluorescence (OH-LIF), Laser Doppler Velocimetry (LDV) and Coherent Anti Stokes Raman Scattering (CARS) to characterize velocity and temperature.

Many numerical simulations of this case have been presented using RANS, [63], and LES, [64-72]. By comparing results, it appears as if the agreement between predictions and experiments has improved over time, and particularly after switching to LES being able to capture the dynamics of the shear layers and the wake. Hex-dominant grids with ~7.4 and 59.2 million cells, with refinement at the walls are used. According to [72] the finer grids do not significantly influence the results.

Figure 2a present volumetric renderings of the density gradient, $\nabla\varrho$, for non-reacting LES using the HV, SMG and LDKM subgrid models. Included is also an experimental Schlieren image to facilitate qualitative comparison of the flow, mixing and shock structures. Oblique shocks are formed at the tip of the wedge that reflect off the upper and lower walls before impinging on the H_2-filled wake. Together with the bent expansion fans, radiating from the base of the wedge, this results in a shock-train. The upper and lower wall boundary layers are influenced by the reflected shocks, resulting increased wall temperature, and thickening of the boundary layer. The wedge boundary layer separates at the base, and shear-layers are formed that roll-up into Kelvin-Helmholtz (KH) vortices. Comparing the LES predictions with the Schlieren image show good agreement for the shock-train and mixing pattern. An effect of the subgrid modeling is seen in the $\nabla\varrho$ images, suggesting that the HV and LDKM models are more accurate than the SMG model that result in an incorrect shock-train. Figure 2b compares cross-sectional profiles of the time-averaged axial velocity, $\langle v_x \rangle$, at five cross sections, x/h=13.0, 20.83, 22.0, 26.16 and 34.5. Results from LES with the SMG, HV and LDKM models are included together with RANS results based on the k-ω model. Only small differences are found in $\langle v_x \rangle$, but with the HV and LDKM models showing better agreement with the experimental data. These differences are however more pronounced for the rms axial velocity fluctuations, v_x^{rms}, as detailed in [72].

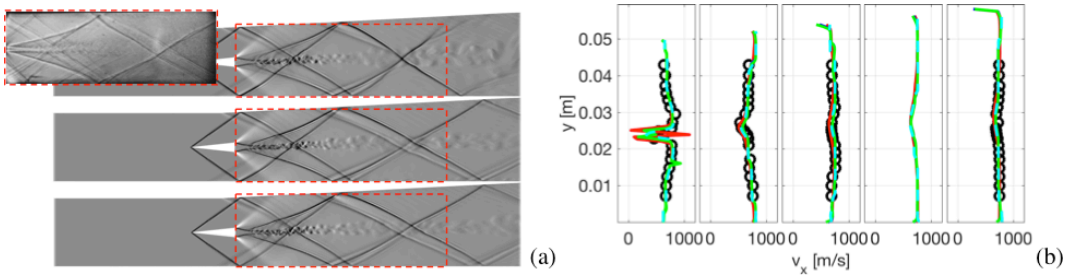

Figure 2. (a) Volumetric renderings of the density gradient, $\nabla\varrho$, for the (a) SMG, (b) HV and (c) LDKM LES predictions for a non-reacting case together with an insert showing an experimental Schlieren image from [60-62]. (b) Profiles of (a) time-averaged axial velocity, $\langle v_x \rangle$, from the non-reacting case at five cross sections, x/h=13.0, 20.83, 22.0, 26.16, and 34.5. Legend: (○) LDV, (—) LES-SMG, (—) LES-HV, (—) LES-LDKM, and (– –) k-ω RANS.

Figures 3a and 3b present volumetric renderings of $\nabla\varrho$ from the side together with the heat-release, Q, for different reaction mechanisms (D7, J20 and Z22) using the LDKM subgrid model, and different LES combustion models (PaSR, TFM and ESF) using the Z22 reaction mechanism and the LDKM subgrid model. Included in figures 3a and 3b are also experimental Schlieren and OH-LIF images to facilitate assessing the flow, mixing and shock-train. With combustion the expansion fans at the corners of the wedge almost disappear, and the recompression shocks become weaker compared to the non-reacting case in figure 2a. Also, the recirculation region becomes longer and wider, and acts as a virtual flameholder, and the peak reverse velocity and base pressure increase compared to the non-reacting case in figure 2a. The shear-layers from wedge corners are more marked in the reacting case, and ignition occurs in these as a result of shock impingement. Concerning the influences of the reaction mechanism we find that the D7 reaction mechanism ignite in the shear-layers because of its too short ignition delay time, figure 1, resulting in too early and very intense heat-release, inhibiting the formation of the KH billows observed in the Schlieren and OH-LIF images, affecting the downstream flow. The J20 and Z22 reaction mechanisms, on the other hand, show delayed ignition and flame stabilization by recirculation of hot gases in agreement with the Schlieren and OH-LIF images. Concerning next the influence of the LES combustion model we find very little difference between the predictions from the LES-ESF and LES-PaSR models, whereas the LES-TFM models results in a less intense flame.

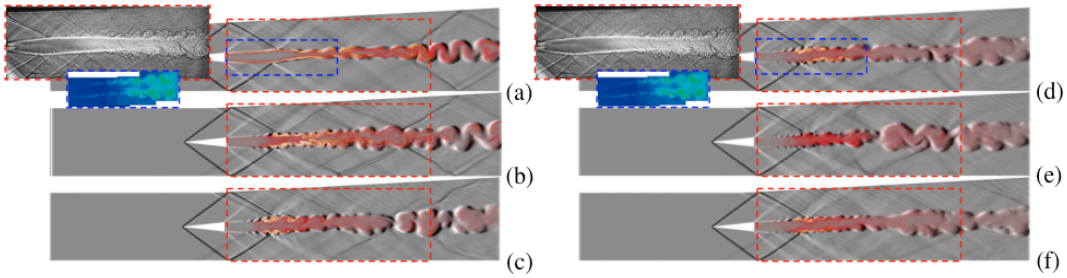

Figure 3. Volumetric renderings from the side of the density gradient, $\nabla\varrho$, combined with the heat-release, Q, for the (a) D7, (b) J20 and (c) Z22 reaction mechanisms using the LDKM subgrid flow model and for the (d) PaSR, (e) TFM and (f) ESF LES combustion model using the detailed Z22 reaction mechanism together with inserts showing experimental Schlieren (top) and OH-LIF (bottom) images of the reacting case from [60-62]. From [46].

Figures 4a and 4b show profiles of $\langle v_x \rangle$ and the time-averaged temperature, $\langle T \rangle$, from the reacting cases at five cross sections, x/h=13.0, 20.83, 22.0, 26.16, and 34.5. At the first station all LES show strong reverse $\langle v_x \rangle$ on each side of the jets and good agreement with the experimental profile, although with the predicted jets being stronger than the measured ones. At the second station the predicted $\langle v_x \rangle$ defect is narrower than the measured one and slightly asymmetric, cf. [61, 65, 68]. At the fourth and fifth stations, good agreement is obtained for $\langle v_x \rangle$, for all LES, resulting in a virtually flat $\langle v_x \rangle$ profile. Concerning $\langle T \rangle$ we notice at the first station that the LES using D7 overpredict $\langle T \rangle$ in the shear-layers, while the LES using J20 and Z22 underpredict $\langle T \rangle$ in the shear-layers. This is consistent with figure 1 showing that D7 ignite too early, whereas J20 and Z22 ignite further downstream in the shear-layers allowing the flame to anchor in the strut wake. At the second station, the J20 and Z22 LES results show good agreement with the experimental profile, whereas the D7 LES prediction results in a different bi-modal $\langle T \rangle$ profile as a result of the intense burning in the shear-layers. At the third and fourth sections no experimental data is available, and here we find that the LES results using J20 and Z22 results in broader $\langle T \rangle$ profiles. At the fifth section the LES prediction using the Z22 reaction mechanism shows the best agreement with the experimental data. Concerning the sensitivity to the LES combustion model we find that the LES-PaSR and ESF models behaves almost identically, but with the LES-TFM resulting in narrower $\langle T \rangle$ profiles as a consequence of the lower heat-release seen in figure 3e.

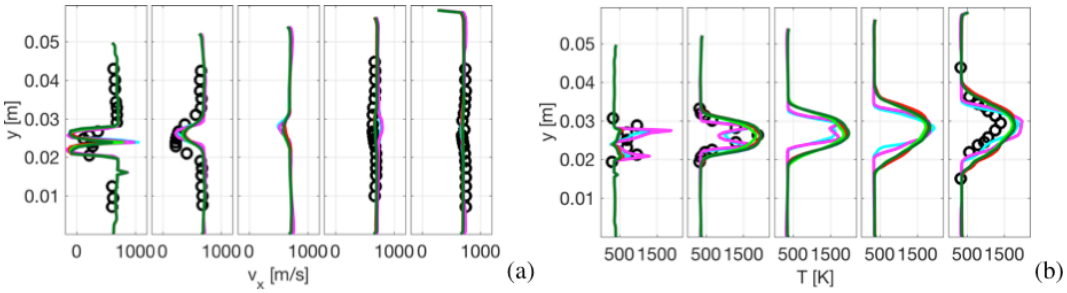

Figure 4. Profiles of the time-averaged axial velocity, $\langle v_x \rangle$, and the time-averaged temperature, $\langle T \rangle$, from the reacting case at five cross sections, x/h=13.00, 20.83, 22.00, 26.16, and 34.50. Legend: (○) LDV and CARS experimental data, (—) LES-PaSR with D7, (—) LES-PaSR with J20, (—) LES-PaSR with Z22, (—) LES-PaSR with Z22, (—) LES-TFM with Z22 and (—) LES-SF with Z22.

5.2. The Fotia & Driscoll Direct Connect Facility Experiments

The Fotia & Driscoll direct connect facility experiments, [73-74], offers an opportunity to study transition from ramjet to scramjet operation, and to further validate the LES models. A constant-area isolator is fed by a two-dimensional Ma 2.2 nozzle, and H_2 is injected at the end of the isolator through a 2.49 mm diameter injector on the centerline, 44.5 mm upstream of the leading edge of a cavity with a slanted downstream wall. A 4° diverging area combustor section starts just after the cavity and discharges into a large-diameter exhaust. An electric heater combined with a hydrogen fueled vitiator was used to provide air stagnation-temperatures between T_0=1040 K and 1500 K at stagnation pressures between p_0=420 kPa to 590 kPa. For the transition studies T_0 and p_0 were fixed at 1400 K and 448.2 kPa, respectively, with the mode transition being facilitated by varying the H_2 inflow, resulting in global equivalence

ratios ranging between ϕ=0.34 (ramjet mode) and 0.19 (scramjet mode), with the three intermediate equivalence ratios of ϕ=0.29, 0.26 and 0.22, representing different stages of the transition.

The computational set-up starts at the Laval nozzle and ends at the combustor exit. Hexahedral grids with ~11 and ~85 million cells, having refinement at the walls and in the cavity, are used. Approximately 87% and 94% of the kinetic energy was resolved rendering both grids appropriate for LES.

Figure 4 present perspective views of the LES predictions of (a) the ramjet Case F1 with ϕ=0.34, (b) the transition Case F3 with ϕ=0.26, and (c) the scramjet Case F5 with ϕ=0.19 in terms of contours of the refractive index gradient, ∇n, iso-surfaces of the second invariant of the velocity gradient, λ_2, (gray) and volumetric renderings of the H_2 mass-fraction (green) and the temperature, T, (warm colors). Based on ∇n we find that the shock-train begins directly after the throat but then develops differently along the isolator depending on ϕ: For high values of ϕ, Case F1, the shock-train is short whereas for low values of ϕ, Case F5, the shock-train is longer. After this region the shock-train gradually disintegrates due to the combined effects of shock-boundary layer interaction, shock-shock interactions and downstream volumetric expansion. As observed by comparing the ∇n distributions, the volumetric expansion increases with increasing ϕ and is higher in the ramjet mode than in the scramjet mode.

The vortical flow, characterized by coherent λ_2 structures, appears to be initiated simultaneously in the upper and lower boundary layers of the isolator just after the end of the shock-train. This behavior suggests that the isolator boundary layer separates in this region, further enforcing the breakdown of the shock-train. The vortical flow then rapidly spreads across the full isolator cross-section, increasing the transverse mixing and simultaneously widening the boundary layer. Just upstream of the cavity, H_2 is injected perpendicular to the main flow direction. This jet-in-cross flow configuration enhances both the transverse and spanwise mixing. Downstream of the H_2 injection and along the cavity the coherent λ_2 flow structures are modified by the vortices from the jet-in-crossflow, the vortices shed from the cavity leading edge, and the heat release from the combustion. An instantaneous image of λ_2 appears chaotic, but averaging λ_2 reveals a horseshoe vortex pair sweeping around the H_2 jet plume and being slightly diverted down into the cavity before breaking up near the end of the cavity. On average, the H_2 plume itself consists of a counter-rotating vortex pair and ring-like vortices surrounding the pair. In addition, boundary layer flow structures (longitudinal and hairpin vortices as well as streaks) also evolve after separation in the isolator, interacting with the plume vortex structures. The refractive index gradient, ∇n show how the density change as a consequence of the longer axial velocity, v_x, penetration and reduced heat release with decreasing ϕ from Case F1 to F5. Note that ∇n is influenced by the H_2 injection, the shock-train, as well as the volumetric expansion from heat release. Moreover, the effective plume angle decreases as the isolator flow speed increases due to the change in volumetric expansion over the cavity. Moreover, we find in all cases that burning occurs in the cavity and along the borders of the H_2 plume. The differences between the λ_2 distributions are associated with the differences in the formation and break-up of the isolator shock-train, being pushed downstream with diminishing ϕ, and the heat-release which also decrease with diminishing ϕ. The temperature, T, increases along the isolator as a consequence of the increase in pressure, p, due to the blockage produced by the volumetric expansion from the heat release. After H_2 injection a large increase in T is observed around the H_2 plume and in

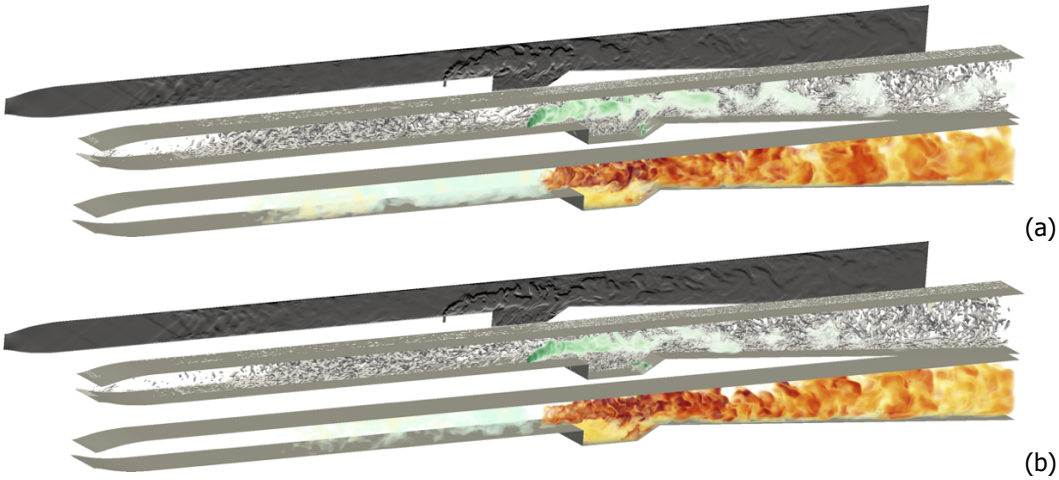

(a)

(b)

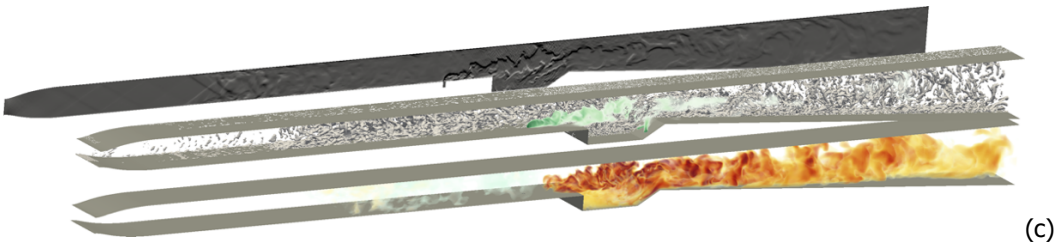

(c)

Figure 5. Perspective views of the flow in terms of the refraction index gradient, ∇n, the 2nd invariant of the velocity gradient, λ_2, (gray) and the H_2 mass-fraction (green), and the temperature, T, (warm colors) for (a) Case F1, (b) Case F3 and (c) Case F5.

the cavity. The cavity acts as a flameholder since hot gases from the trailing edge of the cavity are re-circulated towards the leading edge where it heats up the shear layer above the cavity. The shear layer then interacts both with the H_2 rich plume and the hot air from the isolator surrounding the plume. The heat release, Q, occurs primarily on the outer edges of the H_2 rich plume but to some extent also in the trailing edge of the cavity where additional H_2 is injected.

Figure 6 compares time-averaged and rms wall pressures, $\langle p \rangle_{wall}$ and p_{wall}^{rms}, from experiment and LES. Angle brackets denote time averaging and the superscript 'rms' denote rms fluctuations. Pressure acts as a marker of the combustion dynamics in a thermally choked flow since any change in Q will result in a change in the shock-train and pressure rise. Reasonable agreement between LES and experimental data is found for $\langle p \rangle_{wall}$, in particular for the trends associated with ϕ, and the transition from ramjet to scramjet mode. The computed profiles of $\langle p \rangle_{wall}$ show a steeper rise halfway through the isolator than the experimental data but do reach the expected levels before and within the cavity. At the trailing edge of the cavity and in the first part of the combustor good agreement with the experimental data is observed. The differences between LES and experiments increase with decreasing ϕ, suggesting that the scramjet Case F5 is burning somewhat too quickly. The peak of p_{wall}^{rms} occurs in the isolator due to the break-down of the shock-train. Based on p_{wall}^{rms} the ramjet case F1 is the steadiest since the reaction-zone is mainly located in the low-speed upstream part of the cavity shear-layer. The scramjet Case F5 is the least steady as the reaction zone is moved further aft in the shear layer. The intermediates Case F3, representing mode transition, appears between the ramjet and scramjet cases.

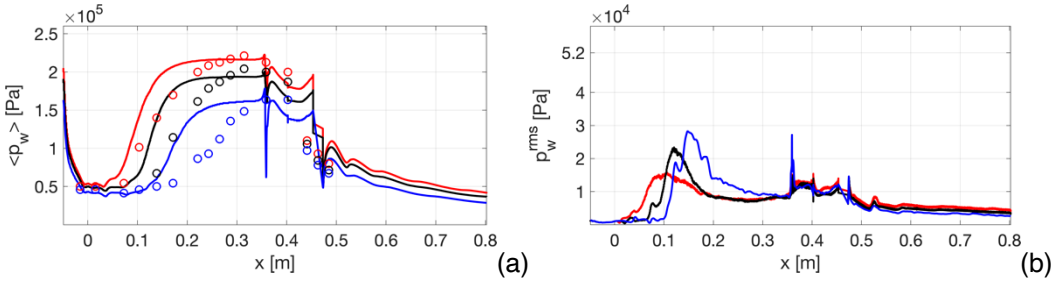

Figure 6. Time-averaged wall pressure (a) and rms wall pressure fluctuations (b) along the lower combustor-wall from experiments, [E1-E2], and the present LES. Legend: Experimental data for case F1 (o), case F3 (o) and case F5 (o), and LES for Case F1 (—), Case F3 (—) and Case F5 (—).

5.3. The Small Scale Flight Experiment (SSFE)

In the EU FP7 project LAPCAT, [75], and the EU H2020 project STRATOFLY, [76], numerical and experimental studies of antipodal hypersonic passenger travel have been performed. In LAPCAT a conceptual flight vehicle model, based on a waverider design, LAPCAT-II MR2, having a dorsal mounted dual mode ramjet engine, was developed, [77]. In STRATOFLY, this model was further developed, resulting in the STRATOFLY MR3 model. For propulsion studies a downscaled version of the LAPCAT-II MR2 model was developed by Langener *et al.*, [78], to be used in the Small-Scale Flight Experiment (SSFE) at the DLR High Enthalpy piston-driven shock tunnel at Göttingen (HEG), [79]. In STRATOFLY this model was further modified to correspond to the STRATOFLY MR3 model. Figure 7a shows a CAD image of the small scale STRATOFLY MR3 model inserted in the test section of the HEG. With this set-up, free-flight tests were carried out at Ma 7.34 at an altitude of 28 km, [80-81]. At these conditions the temperature, density and velocity are T=264 K, ϱ=0.0272 kg/m^3 and v=2398 m/s. In the SSFE the downscaled STRATOFLY MR3 model is suspended in the test-section by two kevlar/aramide cords. Each cord is arranged in

a V-configuration passing through the SSFE model and is then attached on either side to the clamping mechanism. To allow free flight tests, the cords are cut exactly when the shock enters the test-section, allowing for ~4 ms test-time before the model is caught by a cradle mechanism. The STRATOFLY MR3 model include a H_2 injection system, pressure transducers and a transparent upper wall enabling wall-temperature or heat-flux measurements using ultra-fast temperature sensitive paint, [82], and line-of-sight integrated species measurements using laser absorption spectroscopy, [81]. Several combined, theoretical, numerical, and experimental studies have recently been published, e.g. [82-83], resulting in an enhanced understanding of the complex flow and combustion physics.

Figure 7b shows the computational SSFE model, which is a downscaled (1:60) and simplified version of the STRATOFLY MR 3 flight vehicle consisting of an inlet, an isolator, a combustor, and an exhaust nozzle. The wings are partially cut to fit the HEG test section, and the combustor is modified to compensate for some of the adverse scaling effects in subscale tests, [78], by means of optimizing the combustor layout and increasing the equivalence ratio to $\phi \approx 1.0$. Fuel injection is performed on the top of the semi-struts in the front of the combustor at the top and bottom of the central injection strut. The computational set-up consists of the HEG test-section with the SSFE model. A hexahedral-dominated grid of ~34 million cells was used for the baseline case, and finer grid with ~272 million cells was developed to study grid sensitivity. Both grids have the same topology, with low resolution in the freestream but are refined along the engine flow path and towards the combustor walls and struts. Approximately 88% and 93% of the kinetic energy was resolved, rendering both grid acceptable.

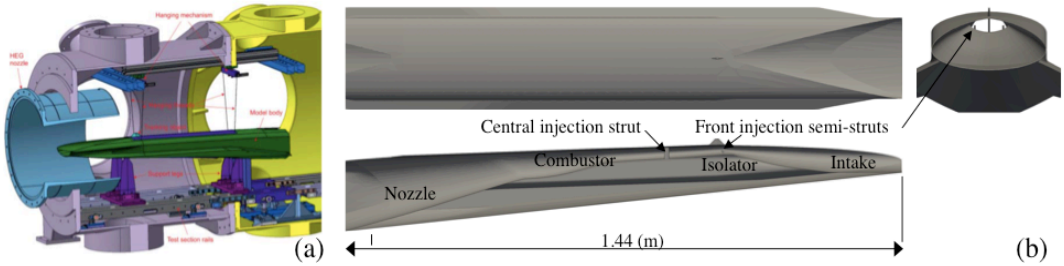

Figure 7. The SSFE. (a) Schematic of the Small Scale Flight Experiment (SSFE) installed in the HEG test section and (b) CAD views of the computational model of the SSFE model.

Figure 8 present exploded views from the side- and top of volumetric rendering of the (a) axial velocity, v_x, (b) temperature, T, (c), pressure, p, (d) heat-release, Q, and (e) species mass fractions, Y_i, from LES of the SSFE experiments. High axial velocities are found across the intake with the exception of a thin boundary layer adjacent to the intake wall. A counter-rotating vortex pair develop at some distance downstream of the intake lip as a result of the laminar to turbulent transition and continues to develop until it reaches the combustor intake. Here, v_x is relatively uniform with the exception of the boundary layer, and the imprint of the counter-rotating vortex pair. The flow separates at the lower wall, between, and just downstream of the semi-struts. This separation is shallow and is initiated at the junction between the downstream part of the intake and the upstream part of the combustor, following the break-up of the intake counter-rotating vortex pair. The H_2 injected on the semi-struts creates two large counter-rotating vortices the dominate the flow during the remaining combustor. The flow between the semi-struts and the full-strut appears very complex, dominated by the large counter-rotating vortices from the struts, the three-dimensional shock-train through the combustor, the combustor boundary layers, and the small-scale turbulence developing from the interacting large-scale processes. Here, only limited volumetric expansion is observed since the H_2 is mixing, and just about to ignite, primarily due to shock impingement. Just after the full strut, a significant decrease in v_x is observed due to large volumetric expansion and increased pressure as a result of the H_2 being fully ignited, resulting in a substantial heat release. Further downstream, and in the nozzle, v_x recovers and increases to levels sufficiently high to provide thrust. The temperature, T, is low all along the intake, except at the walls where it increases slightly due to friction, and in the combustor inlet where T increases slightly due to compression. After the semi-struts, where H_2 is injected, T increases once the injected H_2 has mixed with the compressed air from the intake. The ignition is due to shock compression, and this results in that the edges of the large-scale vortices created by the semi-struts burn intensely at high T. When additional H_2 is injected sideways from the full-strut ignition occurs throughout the cross-section, and T increases to around 2500 K across the whole cross-section. Further downstream and in the nozzle T gradually decrease due

to the expansion facilitated by the combustor and nozzle shape. Throughout the combustor and nozzle, the large-scale vortices dominate the flow, mixing and small-scale turbulence generation.

The pressure, p, shows clear imprints of the three-dimensional shock train developing in the combustor, and particularly downstream of the full strut, where the effects of the large-scale vortical structures starts to mutually interact with the pressure through baroclinic torque and vortex stretching, influencing mixing at all resolved scales. The high p region ends where the constant area combustor change into the diverging area combustor section, where the flow starts to accelerate. The shock-train is still present

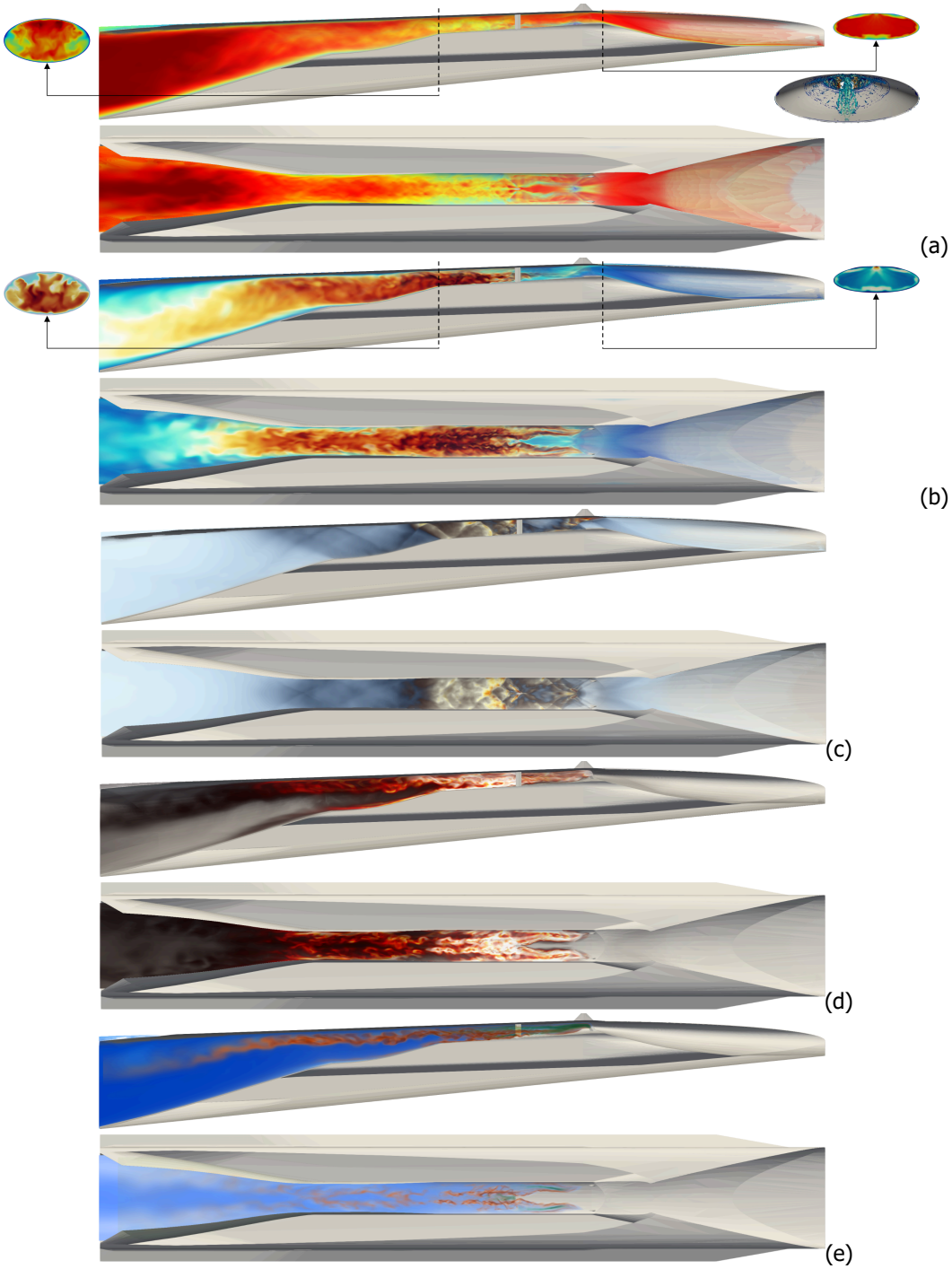

Figure 8. Side- and top views from the combustion LES of the SSFE in terms of (a) axial velocity, v_x, (b) temperature, T, (c), pressure, p, (d) heat-release, Q, and (e) species (H_2, OH and H_2O) distributions. Two additional cross sections at the combustor intake (x=0.42 m) and at the end of the constant combustor cross-sections (x=0.90 m) are also included at the right and left, respectively, to facilitate the understanding of the three-dimensional flow.

along diverging area combustor section, and into the nozzle but rapidly decreases in strength. The p-waves influence the chemical reaction rates which are enhanced in the constant area combustor, promoting heat release, Q, which occurs on the edges of the H_2 plumes once the H_2 has mixed properly with the ingested air. The majority of Q is found just after H_2 has been injected sideways from the full strut, resulting in complete combustion across the combustor. The species, H_2 in green, OH in magenta, H_2O in blue and remaining radicals in orange, distributions essentially follow the flow through the constant area and diverging area combustor sections, and leave a feeble trace of unburnt H_2, OH, and radicals towards the upper wall. Most species are deeply embedded in the primary longitudinal vortex structures, interfered only but the shock trains and the chemical reactions. Due to the high turbulence levels, tur bulent mixing is extremely efficient and promotes combustion.

Figure 9 shows images from (a) experiments and (b) LES of the wall heat flux on the lower combustor wall (left panel) and on the intake surface (right panel), as well as (c) the wall pressure along the upper combustor surfaces as indicted. Regarding the wall heat flux the same colormaps are employed for the experimental and LES images on each section but different colormaps are used for the upper combustor wall and intake surface. The measured wall heat flux image for the intake surface is obtained from [82] whereas those of the lower combustor wall are provided by DLR as part of STRATOFLY. For the intake the wall surface heat flux increases downstream of the flat portion between the inlet lip and the downstream curved intake due to the compression of the flow. Imprints of the vortex pair close to the center plane and observed in figures 9a and 9b can be seen in both the experimental and computational images. For the lower combustor wall the differences between the experimental and computational results are larger but the trends are similar with a region of high wall heat flux between the two semi struts and the full strut. Regarding the wall pressure, p_w, normalized by the free stream total pressure, p_t, in figure 9c, results from the non-reacting and reacting cases are included together with the Rayleigh line. For the reacting case two peaks at x≈0.47 m and 0.65 m can be seen, these corresponds to the pressure increase due to injection at the semi-struts and full struts, respectively. The increase in p_w between x≈0.55 m and 0.90 m is due to the volumetric expansion caused by the exothermicity of combustion and is reasonably reproduced by the LES. Both the experimental and computed peak pressures exceeds the maximum theoretical pressure rise due to H_2-air combustion indicated by the Rayleigh-line, suggests the presence of a strong shock-train throughout the combustor.

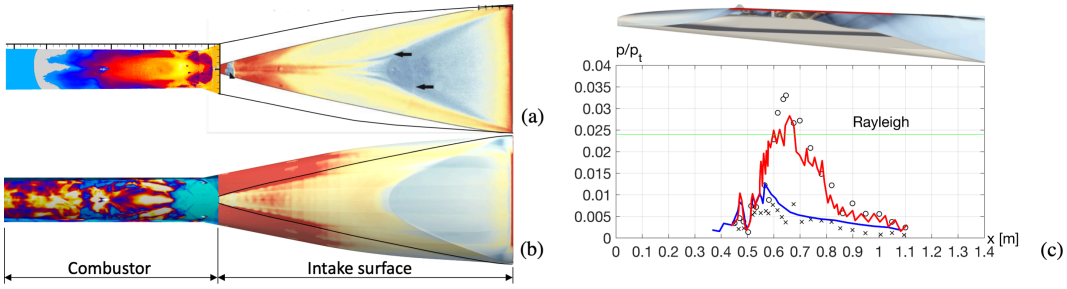

Figure 9. Measured (a) and computed (b) wall heat flux on the lower combustor wall and on the intake. The same colormaps are used for the measured and computed images on each part but different colormaps are used for the lower combustor wall and intake. The experimental wall heat-flux image for the intake is obtained from [82] whereas those of the lower combustor wall are provided by DLR. In figure (c) experimental (symbols) and computed wall pressures, p_w, normalized by the free stream total pressure, p_t, are presented for a non-reacting case (blue) and a reacting case (red) along the highlighted line.

Figure 10 compare cross sectional profiles of the time-averaged axial velocity, $\langle v_x \rangle$ temperature, $\langle T \rangle$, and mass fractions $\langle Y_{H2} \rangle$, $\langle Y_{OH} \rangle$, $\langle Y_{H2O} \rangle$ and $\langle Y_{NO} \rangle$ at x=0.395, 0.550, 0.700, 0.800, 0.900 and 1.100 m along the combustor. The highest $\langle v_x \rangle$ occur over the intake and the nozzle whereas lower $\langle v_x \rangle$ prevail in the combustor as a consequence of the complex flow pattern and the volumetric expansion due to the exothermicity. The wakes of the semi struts appear clearly in $\langle v_x \rangle$ at x=0.550, and of the full strut at x=0.700, after which the $\langle v_x \rangle$ deficit has disappeared due to the volumetric expansion that gradually increase $\langle v_x \rangle$ further downstream. $\langle T \rangle$ is close to the freestream value over the intake, x=0.395, with some increase observed in the boundary layers due to friction heating. Just downstream of the semi struts, at x=0.550, $\langle T \rangle$ increases along the edges of the injected $\langle Y_{H2} \rangle$ plume as it ignites. This is particularly evident on the outer edges of the $\langle Y_{H2} \rangle$ plumes. Further downstream, at x=0.550 to 0.900, the full com-

bustor cross-section is ignited, resulting in high $\langle T \rangle$ across the full engine duct. Further downstream, at x=1.100 $\langle T \rangle$ decrease somewhat due to the widening the nozzle and the flow acceleration. The imprints of the $\langle Y_{H2} \rangle$ injection from the two semi struts and the combustion occurring on the edges of the $\langle Y_{H2} \rangle$ plumes from two semi-struts can easily be seen. The rapid spread of combustion across the combustor cross-section is also evident just downstream of the full strut. $\langle Y_{OH} \rangle$ is formed where combustion, heat release, and volumetric expansion occurs, and high values of $\langle Y_{OH} \rangle$ are found at the boundaries of the $\langle Y_{H2} \rangle$ plumes, at x=0.550, and just after the full strut, x=0.700, where the sideways injected H_2 promotes complete combustion across the full width of the engine duct. $\langle Y_{OH} \rangle$ gradually diminish further downstream, at x=0.800 and 0.900 as combustion becomes complete as at x=1.100, where $\langle Y_{OH} \rangle$ is zero. $\langle Y_{H2O} \rangle$ is non-existing over the intake but form as soon as combustion has started on the edges of the $\langle Y_{H2} \rangle$ plumes at x=0.550 and continues to form with downstream distance from H_2 injection. Based on $\langle Y_{H2O} \rangle$ complete combustion has occurred just after x=0.800, where the computed $\langle Y_{H2O} \rangle$ profiles are virtually flat across the engine duct. Comparing with the experimentally measured line-of sight-integrated $\langle Y_{H2O} \rangle$ values excellent agreement is observed between x=0.550 and 1.100. Regarding NO very good agreement between the experimentally measured line-of sight-integrated $\langle Y_{NO} \rangle$ values and the computed $\langle Y_{NO} \rangle$ values is observed, shown reciprocal validation of the LES and experiments.

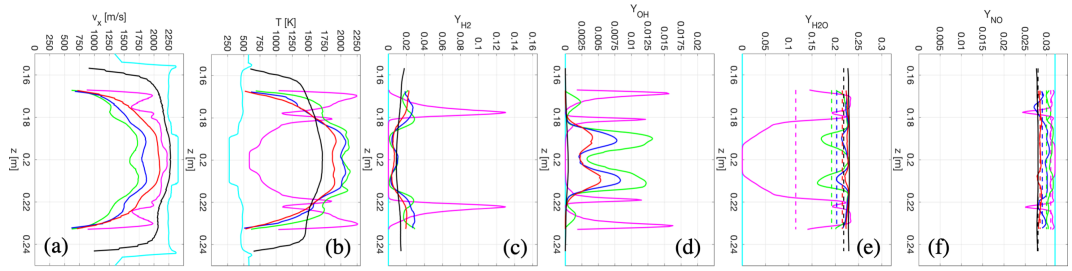

Figure 10. Cross sectional profiles of the time-averaged (a) axial velocity, $\langle v_x \rangle$, (b) temperature, $\langle T \rangle$, as well as the mass fractions (c) $\langle Y_{H2} \rangle$, (d) $\langle Y_{OH} \rangle$ and (e) $\langle Y_{H2O} \rangle$ at x=0.395 (—), 0.550 (—), 0.700 (—), 0.800 (—), 0.900 (—) and 1.100 (—) m along the combustor.

Concluding Remarks

Predictive modeling of high-speed combustion is becoming increasingly important for the development of novel air-breathing propulsion systems such as ramjet, scramjet and dual-mode ramjet engines. The increase in computational capacity in the past decade has made many of these flows numerically accessible. However, the interaction of turbulence with physical processes, such as spray dynamics, vaporization, chemical kinetics, convective and radiative heat-transfer etc., is a great challenge. Major advances in modeling turbulent flow are now made possible with the development of Large Eddy Simulation (LES) and similar methods. The philosophy of LES is to explicitly solve for the large (energetic) scales of the flow, directly affected by boundary conditions, whilst modeling the small (less energetic) scales of the flow. For historical and practical reasons, the development of LES models is however still based on ideas inherited from RANS models, resulting in improved predictions, due mainly to that in LES the large turbulence scales are resolved. However, to meet the future demands in more accurate, fast, reliable and detailed predictions of engineering applications improvements to the LES methodology will be necessary. In this author's opinion, the most critical areas that needs to be addressed are: (i) improved subgrid models for compressible flows, including shock-shock, shock-boundary-layer and shock-interface interactions; (ii) upgraded models for the filtered reaction rates in compressible chemically reactive flows, and (iii) improved spray combustion models. In addition, the different communities using and developing LES should start to engage in cross-disciplinary activities such as systematic validation of models and methods. The future of LES for high-speed combustion applications is promising, in particular if the LES results are analyzed together with experimental data. This, in turn, puts pressure on the development of both experimental facilities and diagnostics, redirecting the experimental work towards fewer but more carefully instrumented experiments. Only by combing experimental data and simulation data can the next generation air-breathing engines be developed to the standard required.

Acknowledgement

This study was supported by the European Union's Horizon 2020 research and innovation program STRATOFLY under grant agreement no. 769246. Computer time was provided by the Swedish National

Infrastructure for Computing, partially funded by the Swedish Research Council through grant agreement no. 2016-07213. The author acknowledges the outstanding Small Scale Flight Experimental work of DLR Göttingen, and in particular the collaboration with Dr. Jan Martinez and his team.

References

[1] Sagaut P.; 2001, "Large Eddy Simulation for Incompressible Flows", Springer Verlag.
[2] Menon S. & Fureby C.; 2010, "Computational Combustion", In Encyclopedia of Aerospace Engineering, Eds. Blockley R. & Shyy W., John Wiley & Sons.
[3] Echekki T. & Mastorakos E.; 2011 (Eds.), "Turbulent Combustion Modeling", Fluid Mechanics and its Applications, 95, Springer Science+Business Media.
[4] Hawkes E.R., Sankaran R., Sutherland J.C. & Chen J.H.; 2005, "Direct Numerical Simulation of Turbulent Combustion: Fundamental Insights Towards Predictive Models", J. Physics: Conference Series, **165**, p 65.
[5] Guiterrez L.F., Tamagno J.P. & Elaskar S.A.; 2016, "RANS Simulation of Turbulent Diffusive Combustion using OpenFoam", J. Appl. Fluid Mech., **9**, p 669.
[6] Ingenito A., Giuseppina De Flora M., Bruno C. & Giacomazzi E. & Steelant J.; 2006, "LES Modeling of Scramjet Combustion". AIAA 2006-1383.
[7] Peterson D M. & Candler, G.V.; 2008, "Hybrid RANS/LES of a Supersonic Combustor", AIAA 2008-6923.
[8] Genin F. & Menon S.; 2009, "Simulation of Turbulent Mixing Behind a Strut Injector in Supersonic Flow", AIAA 2009-0132.
[9] Koo H., Donde P. & RamanV.; 2013, "LES-based Eulerian PDF Approach for the Simulation of Scramjet Combustors", Proc Comb. Inst. **34**, p 2093.
[10] Fureby C., Nordin-Bates K., Petterson K., Bresson A. & Sabelnikov V.; 2014, "A Computational Study of Supersonic Combustion in Strut Injector and Hypermixer Flow Fields", Comb. Inst. **35**, p 2127.
[11] Moule Y, Sabelnikov V, Mura A, Smart M.; 2014, "Computational Fluid Dynamics Investigation of a Mach 12 Scramjet Engine", J. Prop. Power, **30**, p 461.
[12] Saghafian A, Terrapon V.E. & Pitsch H.; 2015, "An Efficient Flamelet-Based Combustion Model for Compressible Flows", Comb. Flame, **162**, p 652.
[13] Fulton J.A., Edwards J.R., Cutler A., McDaniel J. & Goyne C.; 2016, "Turbulence/Chemistry Interactions in a Ramp-Stabilized Supersonic Hydrogen-Air Diffusion Flame", Comb. Flame, **174**, p 152.
[14] Nordin-Bates K., Fureby C., Karl S. & Hannemann K.; 2017, "Understanding Scramjet Combustion using LES of the HyShot II Combustor", Proc. Comb. Inst., **36**, p 2893.
[15] Lacaze G., Vane Z. & Oefelein J.C.; 2017, "Large Eddy Simulation of the HIFiRE Direct Connect Rig Scramjet Combustor", AIAA 2017-0142.
[16] Fedina E., Fureby C., Bulat G. & Maier W.; 2017, "Assessment of Finite Rate Chemistry Large Eddy Simulation Combustion Models", Flow, Turb. and Comb., **99**, p 385.
[17] Fureby C.; 2018, "The Volvo Validation Rig – A Comparative Study of Large Eddy Simulation Combustion Models at Different Operating Conditions", AIAA 2018-0149.
[18] Ferri A.; 1973, "Mixing-Controlled Supersonic Combustion", Annu. Rev. Fluid Mech., **5**, p 301.
[19] Curran E.T., Heiser W.H. & Pratt D.T.; 1996, "Fluid Phenomena in Scramjet Combustion Systems", Annu. Rev. Fluid Mech., **28**, p 323.
[20] Erlebasher G., Hussaini M., Special C. & Sang T.; 1992, "Towards the Large Eddy Simulation of Compressible Turbulent Flows", J. Fluid Mech., **238**, p 155.
[21] Kim W.-W. & Menon S.; 1995, "A New Dynamic One Equation Subgrid-scale Model for Large Eddy Simulations", AIAA 95-0356.
[22] Cook A.W. & Cabot W.H.; 2005, "Hyperviscosity for Shock-Turbulence Interactions". J. Comp. Phys., **203**, p 379.
[23] Branley N & Jones W.P.; 2001, "Large Eddy Simulation of a Turbulent Non-Premixed Flame", Comb. Flame, **127**, p 1914.
[24] Peters N.; 2000, "Turbulent Combustion", Cambridge University Press.
[25] Fureby C.; 2000, "Large Eddy Simulation of Combustion Instabilities in a Jet-Engine Afterburner Model", Comb. Sci & Tech, **161**, p 213.
[26] Saghafian A., Tarrapon V. & Pitsch H.; 2015, "An Efficient Flamelet-Based Combustion Model for Compressible Flows", Comb. Flame, **162**, p 652.
[27] Colin O., Ducros F., Veynante D. & Poinsot T.; 2000, "A Thickened Flame Model for Large Eddy Simulation of Turbulent Premixed Combustion", Phys. Fluids., **12**, p 1843.

[28] Fureby C.; 2009, "LES Modeling of Combustion for Propulsion Applications", Phil. Trans. R. Soc. A, **367**, p 2957.
[29] Giacomazzi E., Bruno C. & Favini B.; 2000, "Fractal Modeling of Turbulent Combustion", Comb. Theory & Modeling, **4**. p 391.
[30] Sabelnikov V. & Fureby C.; 2013, "LES Combustion Modeling for High Re Flames using a Multi-phase Analogy", Comb. Flame, **160**, p 83.
[31] Gao F. & O'Brian E.; 1993, "A Large Eddy Simulation Scheme for Turbulent Reacting Flows", Phys Fluids A, **5**, p 1282.
[32] Jones W.P., Marquis A.J. & Wang F.; 2015, "Large Eddy Simulation of a Premixed Propane Turbulent Bluff Body Flame using the Eulerian Stochastic Field Method", Fuel, **140**, p 514.
[33] Menon S., 2000, "Subgrid Combustion Modeling for Large Eddy Simulations", Int. J. Engine Res., **1**, p 209.
[34] Nilsson T. & Fureby C.; 2021, "LES of H2-air Jet Combustion in High Enthalpy Supersonic Cross-flow", Phys. Fluids, **33**, 035133.
[35] Magnussen B.F.; 1981, "On the Structure of Turbulence and Generalized Eddy Dissipation Concept for Chemical Reactions in Turbulent Flow", 1981-0042.
[36] Chomiak J.; 1970, "A Possible Propagation Mechanism of Turbulent Flames at High Reynolds Numbers", Comb. Flame, **15**. p 319.
[37] Batchelor G.K. & Townsend A.A.; 1949, "The Nature of Turbulent Motion at Large Wave-numbers", Proc. Roy. Soc. London A, **199**, p 238.
[38] Kawai S. & Lele S.K.; 2008, "Localized Artificial Diffusivity Scheme for Discontinuity Capturing on Curvilinear Meshes," J. Comp. Phys., **227**, p 9498.
[39] Adams N.A. & Shariff K.; 1996, "A High-Resolution Hybrid Compact-ENO Scheme for Shock-Turbulence Interaction Problems," Journal of Computational Physics, **127**, p 27.
[40] Strang G.; 1968, "On Construction and Comparison of Difference Schemes", SIAM J. Num. Anal., 5, p 506.
[41] Hairer E. & Wanner G.; 1991, "Solving Ordinary Differential Equations", II: Stiff and Differential-Algebraic Problems, 2nd Ed., Springer Verlag.
[42] Kurgaonov A. & Tadmor E.; 2000, "New High Resolution Central Schemes for Nonlinear Conservation Laws and Convection-Diffusion Equations", J. Comp. Phys., **160**, p 241.
[43] Kurgaonov A., Noelle S. & Petrova G.; 2001, "Semidiscrete Central Upwind Schemes for Hyperbolic Conservation Laws and Hamilton Jacobi Equations", SIAM J. Sci. Comp., **23**, p 707.
[44] Philips G.M. & Taylor P.J.; 1996, "Theory and Applications of Numerical Analysis", Academic Press.
[45] Fedina E., Fureby C., Bulat G. & Maier W.; 2017, "Assessment of Finite Rate Chemistry Large Eddy Simulation Combustion Models", Flow, Turb. and Comb., **99**, p 385.
[46] Zettervall N. & Fureby C.; 2018, "A Computational Study of Ramjet, Scramjet and Dual-mode Ramjet Combustion in Combustor with a Cavity Flameholder", AIAA 2018-1146.
[47] Marinov N.M., Westbrook C.K. & Pitz W.J.; 1995, "Detailed and Global Chemical Kinetics Model for Hydrogen", 8th Int. Symp. on Transport Properties, San Fransisco, CA, USA.
[48] Eklund D.R. & Stouffer S.D.; 1994, "A Numerical and Experimental Study of a Supersonic Combustor Employing Swept Ramp Fuel Injectors", AIAA 94-2819.
[49] Baurle R.A. & Girimaji S.S.; 2003, "Assumed PDF Turbulence-Chemistry Closure with Temperature Composition Correlations", Comb. Flame, **134**, p. 131.
[50] Davidenko D.M., Gökalp I., Dufour E. & Magre P.; 2003, "Numerical Simulation of Hydrogen Supersonic Combustion and Validation of Computational Approach", AIAA 2003-7003.
[51] Jachimowski C.J.; 1988, "An Analytical Study of the Hydrogen–air Reaction Mechanism with Application to Scramjet Combustion", NASA-TP-2791.
[52] Alekseev V.A., Christensen M. & Konnov A.A.; 2015, "The Effect of Temperature on the Adiabatic Burning Velocities of Diluted Hydrogen Flames: A Kinetic Study using an Updated Mechanism", Comb. Flame, **162**, p. 1884.
[53] Wang H., You X., Joshi A.V., Davis S.G., Laskin A., Egolfopoulos F. & Law C.K.; 2007, "USC Mech. Version II. High-Temperature Combustion Reaction Model of H2/CO/C1-C4 Compounds", Mechanism and additional information is available at http://ignis.usc.edu/USC_Mech_II.htm.
[54] Slack M. & Grillo A.; 1977, "Investigation of Hydrogen-Air Ignition Sensitized by Nitric Oxide and by Nitrogen Oxide", NASA Report CR-2896.
[55] Samuelsen S., McDonell V., Greene M. & Beerer D.; 2006, "Correlation of Ignition Delay with

Natural Gas and IGCC type Fuels", 2006, DOE Award Number: DE-FC26-02NT41431.
[56] Snyder A.D., Robertson J., Zanders D.L. & Skinner G.B.; 1965, "Shock Tube Studies of Fuel-Air Ignition Characteristics", Report AFAPL-TR-65-93-1965
[57] Kwon O.C. & Faeth G.M.; 2001, "Flame/Stretch Interactions of Premixed Hydrogen-Fueled Flames: Measurements and Predictions", Comb. Flame, **124**, p 590.
[58] Dowdy D.R., Smith D.B., Taylor S.C. & Williams A.; 1990, "The Use of Expanding Spherical Flames to Determine Burning Velocities and Stretch Effects in Hydrogen-Air Mixtures", Proc. Comb. Inst., **23**, p 325.
[59] Juniper M., Darabiha N. & Candel S.; 2003, "The Extinction Limits of a Hydrogen Counterflow Diffusion Flame above Liquid Oxygen", Comb. & Flame, **135**, p 87.
[60] Waidmann W., Alff F., Brummund U., Böhm M., Clauss W. & Oschwald M.; 1995, "Supersonic Combustion of Hydrogen/Air in a Scramjet Combustion Chamber", Space Tech. **15**, p 421.
[61] Oschwald M., Guerra R. & Waidmann W.; 1993, "Investigation of the Flowfield of a Scramjet Combustor with Parallel H2-Injection through a Strut by Particle Image Displacement Velocimetry", Int. Symp. On Special topics in Chem. Prop., p 498, May 10-14, Schweveningen, NL.
[62] Waidmann W., Brummund U. & Nuding J.; 1995, "Experimental Investigation of Supersonic Ramjet Combustion (SCRAMJET)", 8th Int. Symp. on Transp. Phenom. In Comb., p 1473.
[63] Oevermann M.; 2000, "Numerical Investigation of Turbulent Hydrogen Combustion in a Scram-jet using Flamelet Modeling", Aerosp. Sci. Tech., **4**, p 463.
[64] Berglund M. & Fureby C.; 2006, "LES of Supersonic Combustion in a Scramjet Engine Model", Proc. Comb. Inst., **31**, p 2491.
[65] Genin F. & Menon S.; 2009, "Simulation of Turbulent Mixing Behind a Strut Injector in Supersonic Flow", AIAA 2009-0132.
[66] Zhouqin F., Mingbo S. & Weidong L.; 2010, "Flamelet/Progress-Variable Model for Large Eddy Simulation of Supersonic Reacting Flow", AIAA 2010-6878.
[67] Potturi A.S. & Edwards J.; 2012, "LES/RANS Simulation of a Supersonic Combustion Experiment", AIAA 2012-0611.
[68] Potturi A.S. & Edwards J.; 2013, "Investigation of Subgrid Closure Models for Finite-Rate Scramjet Combustion", AIAA 2013-2461.
[69] Fureby C., Fedina E. & Tegnér J.; 2014, "A Computational Study of Supersonic Combustion behind a Wedge-shaped Flameholder", J. Shock Waves, **24**, p 41.
[70] Changmin C., Taohong Y. & Majie Z.; 2015, "Large Eddy Simulation of Hydrogen/air Scramjet Combustion using Tabulated Thermo-Chemistry Approach", Chinese J. Aeronautics, **28**, p 1316.
[71] Huang Z.-W., He G.-Q., Qin F., Wei X.-G.; 2015, "Large Eddy Simulation of Flame Structure and Combustion Mode in a Hydrogen Fueled Supersonic Combustor", Int. J. Hydrogen Energy, **40**, p 9815.
[72] Fureby C.; 2019, "A Comparative Study of Subgrid Models, Reaction Mechanisms and Combustion Models in LES of Supersonic Combustion", AIAA J., **59**, p 215.
[73] Fotia M.L. & Driscoll J.F.; 2012, "Isolator–Combustor Interactions in a Direct-Connect Ramjet-Scramjet Experiment", J. Prop. Power, **28**, p 83.
[74] Fotia M.L. & Driscoll J.F.; 2013, "Ram-Scram Transition and Flame/Shock-Train Interactions in a Model Scramjet Experiment", J. Prop. Power, **29**, p 261.
[75] Steelant J., Varvill R., Defoort S., Hanneman K. & Marini M.; 2015, "Achievements Obtained for Sustained Hypersonic Flight within the LAPCAT-II Project", AIAA 2015-3677.
[76] Viola N., Fusaro R., Saracoglu B., Schram C., Grewe V., Martinez J., Marini M., Hernandez S., Lammers K., Vincent A., Hauglustaine D., Liebhardt B., Linke G. & FurebyC.; 2021, "Main Challenges and Goals of the H2020 STRATOFLY Project", Aerotecnica Missili & Spazio, 100, p 95.
[77] Langener T. & Steelant J., 2014, "The LAPCAT MR2 Hypersonic Cruiser Concept", 29th Congress of the International Council of the Aeronautical Sciences, St. Petersburg, Russia, Sept. 7-12.
[78] Langener T. Steelant J., Karl S. & Hannemann K.; 2012, "Design and Optimization of a Small Scale M=8 Scramjet Propulsion System", Space Propulsion 2012, 7-10 May, Bordeaux, France.
[79] Hannemann K. & Martinez Schramm J.; 2007, "High Enthalpy, High Pressure Short Duration Testing of Hypersonic Flows", In: Springer Handbook of Experimental Fluid Mechanics, p. 1081, Springer Berlin Heidelberg, Eds.: Tropea C., Foss J. & Yarin, A.
[80] Hannemann K., Martinez Schramm J., Laurence S. & Karl S.; 2015, "Shock Tunnel Free Flight Force Measurements using a Complex Model Configuration", 8th European Symp. on Aerothermodyna-mics for Space Vehicles, 2-6 March, Lisbon, Portugal.

[81] Jan Martinez, 2021, "Experimental Investigations on Hypersonic Combustion in a Large-scale High Enthalpy Short Duration Facility", von Karman Lecture Series, Stratospheric Flying Opportunities for High-Speed Propulsion Concepts, 25-26 May, The von Karman Institute.
[82] Martinez Schramm J., Karl S., Hannemann K. & Ozawa H.; 2018, "Ultra-fast Temperature Sensitive Paint Shock Tunnel Heat Flux Measurements on the Intake of the LAPCAT II Small Scale Flight Experiment Configuration", HiSST, 26-29 November, Moscow, Russia.
[83] Karl S. & Steelant J.; 2018, "Crossflow Phenomena in Streamline-Traced Hypersonic Intakes", J. Prop. Power, **34**, p 449
[84] Karl S., Martinez Schramm J. & Hannemann K.; 202, "Post-Test Analysis of the LAPCAT-II Subscale Scramjet", CEAS Space Journal, **12**, p 385.